Research Article

Kangning Liu*, Sheliang Wang, Ergang Xiong, Xiaoyi Quan, Jing Wu, Jin Xu, and Nan Zhao

Effect of molybdenum tailings aggregate on mechanical properties of engineered cementitious composites and stirrup-confined ECC stub columns

https://doi.org/10.1515/rams-2023-0110
received February 27, 2023; accepted July 26, 2023

Abstract: Engineered cementitious composites (ECC) exhibit behaviors of multiple cracking and strain-hardening compared to ordinary concrete. However, the use of ultrafine silica sand (S) to produce ECC results in increased cost and environmental overload. This study was to develop an eco-friendly and cheaper ECC by incorporating different replacement ratios of industrial byproduct molybdenum tailings (MT). The mechanical properties of ECC with MT were evaluated. Based on industrial computer technology, nuclear magnetic resonance, and scanning electron microscope techniques, the three-dimensional spatial distribution and fluid distribution of pores and the microstructure of the ECC were investigated, respectively. The mechanical properties of stirrup-confined ECC stub columns were also investigated. Results indicated that the ECC incorporating 25% MT exhibited the best mechanical properties, in which the tensile strength (f_t) increased by 32.16% and exhibited well strain-hardening behaviors. Under a 25% MT replacement ratio, ECC had the lowest porosity and good interfacial transition zone, and bonding interface between polyvinyl alcohol (PVA) fiber (PF) and matrix. Moreover, the stirrup-confined ECC stub column with 25% MT can ensure better both the peak stress (f_{cc}) and peak strain (ε_{cc}). The assessment of environmental impact and cost further indicated that the incorporation of MT to prepare ECC is a promising method.

Keywords: molybdenum tailings, engineered cementitious composites, mechanical properties

1 Introduction

Engineered cementitious composites (ECC), a kind of fiber-reinforced cementitious composites, have ultra-high tensile ductility and saturated multiple cracking behaviors [1–3]. Generally, the deformability (tensile strain) of ECC could reach 1–8%, which makes the application prospect of ECC better than that of ordinary concrete. Moreover, the raw material silica sand (S) used for ECC is more expensive than that of river sand, which increases the production cost of ECC [4]. Meanwhile, with the concept of green building strongly promoted, clean development of high-performance and eco-friendly ECC is a new direction for the development of the construction industry.

To reduce the cost and achieve sustainable development of ECC, some industrial wastes have been tried as raw materials for the preparation of ECC [5,6]. For example, Xu *et al.* [7,8] incorporated artificial geopolymer as aggregate (GPA) to produce ECC and found that exhibit the cost-efficiency and sustainability of GPA-ECC, which provided a sustainable approach for enhancing the long-term tensile performance of high-strength ECC based on artificial aggregates. Zhang *et al.* [9] reported that when S was replaced by crumb rubber, the ductility of ECC increased, but the strength was reduced by about 35%. Li and Yang [10] found that the ductility of ECC was improved by replacing S with recycled fine aggregates of different particle sizes for the preparation of ECC. Similarly, Huang *et al.* [11] prepared ECC by incorporating iron ore tailings with different particle sizes as aggregate and reported that when the particle size of iron ore tailings used was within a reasonable

* **Corresponding author: Kangning Liu,** School of Civil Engineering, Xi'an University of Architecture & Technology, Xi'an 710055, China, e-mail: lkn@xauat.edu.cn
Sheliang Wang: School of Civil Engineering, Xi'an University of Architecture & Technology, Xi'an 710055, China; School of Science, Xi'an University of Architecture and Technology, Xi'an 710055, China
Ergang Xiong: School of Civil Engineering, Chang'an University, Xi'an 710061, Shaanxi, China
Xiaoyi Quan, Jing Wu, Jin Xu: School of Civil Engineering, Xi'an University of Architecture & Technology, Xi'an 710055, China
Nan Zhao: School of Science, Xi'an University of Architecture and Technology, Xi'an 710055, China

range, ECC could obtain the same mechanical properties as conventional ECC. Turk and Demirhan [12] incorporated 100% limestone powder as aggregate to produce ECC and found that the mechanical properties of ECC were enhanced. Adesina and Das [4] incorporated glass with different replacement levels as aggregate to produce ECC and found that when S was replaced by glass aggregate, the mechanical properties of ECC did not deteriorate, and the embodied carbon and cost were reduced by 5.9 and 16.6%, respectively. It was found that using industrial byproducts to produce ECC can not only improve performance but also solve the problem of waste disposal, reduce production costs, and achieve cleaner production of ECC.

Molybdenum tailings (MT) are inevitable industrial byproducts of raw ore refining [13] and are considered to be one of the main pollution sources causing environmental degradation [14,15]. It was reported that approximately 36 million tons of MT are discharged per year in China [16], and the emissions from mine tailings in other countries are increasing year by year [17–19]. A large number of MT are treated by open-air stacking and landfilling, which not only take up a lot of land but also result in soil erosion, and air and water pollution [20–22]. Moreover, there is a risk of mudslides caused by the failure of tailings dams. Hence, the reuse of MT is very key to reducing environmental pollution and the healthy development of the mining industry [23,24].

Various methods of reuse of MT have been proposed to prevent further environmental degradation, such as processing glass ceramics [25], extraction of useful substances again [26,27], growing plants through improvement [28], and processing building materials [29,30]. It is worth noting that with the rapid development of the construction industry, the application of concrete and mortar can consume the largest amount of MT compared to other technologies of MT reuse. Jung and Jeong [29] developed an admixture for high-fluidity concrete by using MT powder and found that MT powder as an admixture can effectively control the flow, viscosity, and strength of high-fluidity concrete when the amount of cement replaced by MT powder was 20%. Siddique and Jang [13] investigated mortar mechanics and durability by incorporating MT as filler material and found that the properties of mortar were improved by mixing with MT, which further confirmed that using MT to prepare building material was a feasible solution for the reuse of MT. Quan *et al.* [16] used MT as fine aggregate to prepare concrete and found that incorporating 60% MT in concrete was the best reuse option for developing green concrete. Similarly, Gao and Guo [31] applied MT to concrete members and made a comprehensive evaluation of stub columns of concrete-filled steel tubes mixed with tailings. The study found that the resource utilization of MT in stub columns of concrete-filled steel tubes had good environmental and cost benefits.

Previous studies found that using MT to prepare cementitious composites is a good cleaner production method. However, to date, there are still few studies about using MT as a fine aggregate to prepare building materials. It is noteworthy that studies on the preparation of ECC using MT have not been found. Thus, to decrease the cost and carbon emission of ECC, and further expand the application of MT in building materials, research on the reuse of MT in ECC is a hot topic and has important environmental and cost benefits.

A comprehensive experimental study on the preparation of ECC using MT as an eco-friendly aggregate was carried out from both mesoscopic and microscopic points of view in this study. First, the crystal composition, microscopic morphology, particle size, and radioactivity of MT were characterized. The uniaxial tension performance, flexural performance, and axial compressive performance of ECC were measured. Additionally, nuclear magnetic resonance (NMR) and industrial computer technology (CT) were used to analyze the pore distribution of ECC to further reveal the influence of MT on the pore structure, after which the microstructure was analyzed using scanning electron microscopy (SEM). Additionally, the stirrup-confined ECC stub column under compression was also investigated.

2 Experimental details

2.1 Materials

The Ordinary Portland Cement (OPC) PO42.5R, silica fume (SF), and first-grade FA as cementitious materials were used. Table 1 provides the chemical composition of the cementitious materials and fine aggregates.

Table 1: Chemical compositions of cementitious materials and fine aggregate (wt%)

	Cementitious materials			Fine aggregates	
	OPC	FA	SF	S	MT
CaO	60.73	3.66	0.44	0.49	4.2
SiO_2	20.85	52.97	97.24	98.63	74.26
Al_2O_3	4.92	29.96	0.19	0.47	5.22
Fe_2O_3	3.59	7.98	0.05	0.49	11.89
MgO	2.87	1.52	0.17	0.14	2.88
SO_3	2.33	0.65	0.78	0.08	0.24
Na_2O	0.25	0.55	—	—	0.22
K_2O	0.46	1.18	0.93	0.08	1.01
TiO_2	0.27	0.49	—	—	—

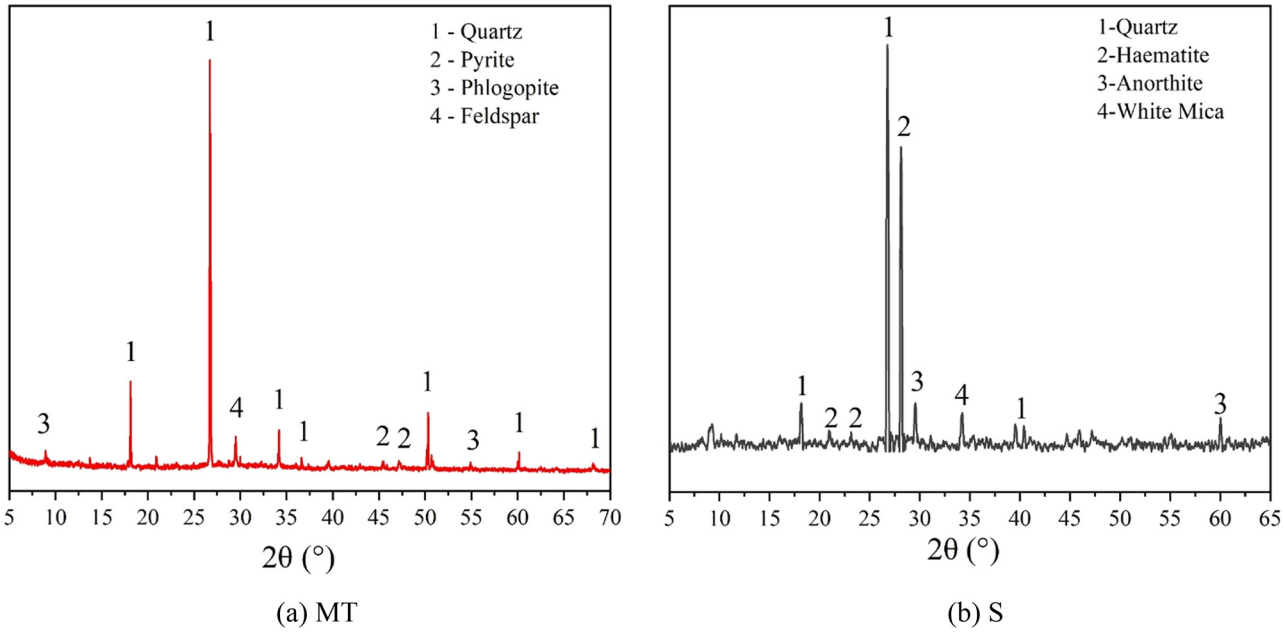

Figure 1: XRD patterns of (a) MT and (b) S.

In this study, the MT from Shaanxi Province, China, and S were used as an aggregate. The main crystal composition and micromorphology of MT and S were determined by X-ray diffraction (XRD) and SEM, as shown in Figures 1 and 2, respectively. It was found from Figures 1 and 2 that the main crystal composition of MT is similar to that of S, which is mainly quartz, and the chemical activity was steady, but MT had more angular surfaces than that of S. In addition, according to the Chinese national standard GB14684-2011, the physical properties of MT and S including apparent density, loose bulk density, crushing index, and water absorption were tested and summarized as listed in Table 2. It can be observed from Table 2 that the crushing index of MT was 9.66% lower than that of S, in which the main reason for this phenomenon is that the particle size of MT is small (Figure 3).

The fiber used was polyvinyl alcohol (PVA) fiber (PF), with its characteristic parameters, are shown in Table 3.

The HRB400 and HPB300 rebar is used for longitudinal and stirrup, respectively. Based on the test standards, some mechanical parameters were obtained by direct tensile testing of the pre-rebar specimens, as shown in Table 4.

2.2 Mix proportions and specimen preparation

2.2.1 Mix proportions

Limited literature had reported the use of MT in concrete and mortar [32,33], and the maximum replacement ratio was set to 100% [16]. However, there are few reports about the utilization of MT in ECC. Thus, to investigate the influence of MT as an eco-friendly aggregate incorporated into ECC and the optimal replacement ratio of MT, only the replacement level of MT was changed. The MT replacement ratio (replace by weight) was 0% (pure S), 25, 50, 75, and 100% (pure MT), respectively. The water/cementitious materials were 0.3, and the aggregate/cementitious materials were 0.5. The volume content of PF was designed to be 2% [11,34]. Five groups' mixed proportions are listed in Table 5.

2.2.2 Specimen preparation

For the preparation of each ECC specimen, in step 1, all the weighed solids were poured into the mixer for mixing, and the mixing was 60 s. In step 2, the water and superplasticizer (SP) were added and stirred for 120 s. In step 3, the PF was slowly added and stirred for 120 s. In step 4, the mixture was put into a mold and vibrated in the 30 s. After consolidation, the molds were removed, and the specimens were placed in the curing box for curing. Figure 4 presents the specimen mixing process.

In this experiment, three parallel specimens for each group were prepared for tests. The cubes specimens (100 mm × 100 mm × 100 mm) were prepared to test the cube compressive strength (f_{cu}). The Φ100 mm (diameter) × 200 mm (high) cylinders were prepared to test the axial compressive strength (f_c) and elastic modulus (E_c). The dog-bone-shaped specimens and 300 mm (length) × 76 mm (width) × 13 mm (thickness) thin

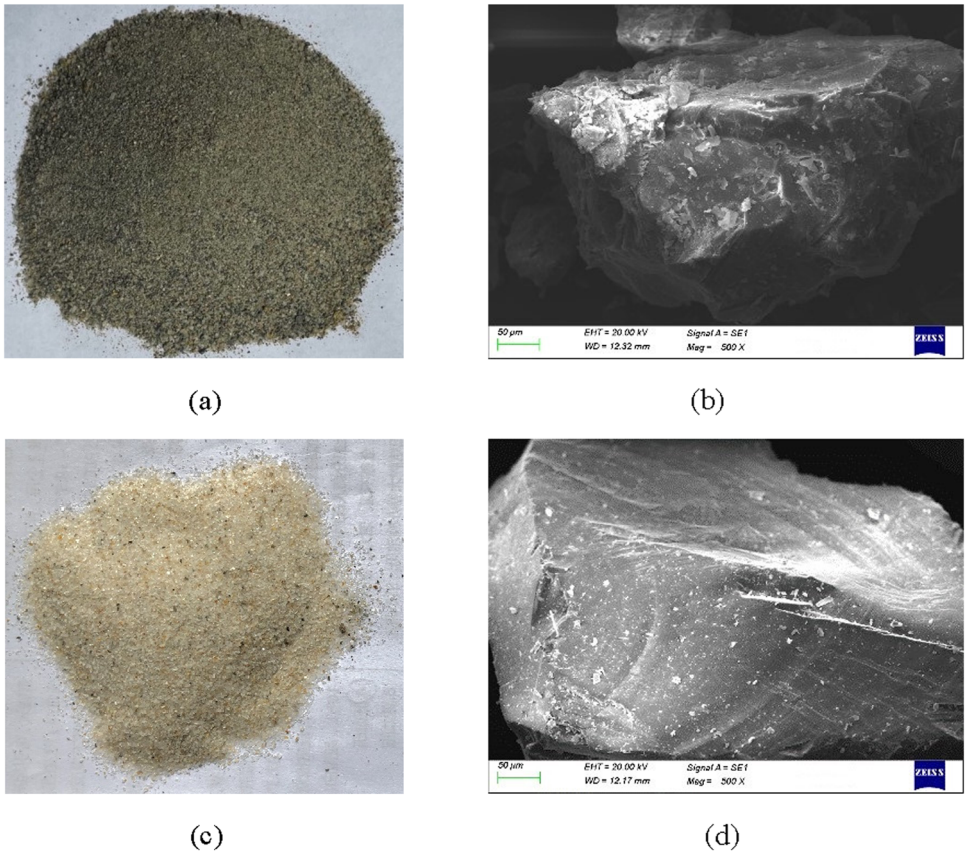

Figure 2: Microscopic structure of MT and S: (a) MT, (b) SEM of MT (enlarged 500 times), (c) S and (d) SEM of S (enlarged 500 times).

slabs were prepared to test the tensile strength (f_t) and flexural strength (f_f), respectively.

The stirrup-confined ECC stub column with different MT was prepared for testing the bearing capacity under axial compression. The dimensions of the stub column are shown in Figure 5. The designation and parameters including dimensions, stirrup ratio of volume, stirrup spacing, and MT replacement ratio of the stub column are listed in Table 6.

2.3 Test methods

2.3.1 ECC mechanical properties testing

Based on the guidance of ASTM E8 and JSCE 2008 universal standards, the dog-bone-shaped specimen was reinforced

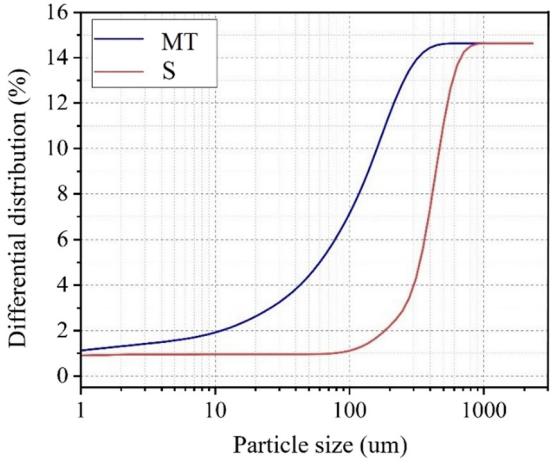

Figure 3: Particle size curve of MT and S.

Table 2: Physical properties of MT and S

	Apparent density (kg·m^{-3})	Loose bulk density (kg·m^{-3})	Crushing index (%)	Water absorption (%)
MT	2,734	1,897	14.86	0.88
S	2,756	1,844	16.45	—

Table 3: Characteristic parameters of fiber

	Length (mm)	Diameter (μm)	Density (g·cm^{-3})	Fracture elongation (%)	Tensile strength (MPa)	Modulus of elasticity (GPa)
PF	12	40	1.3	7	1,600	42

Table 4: Characteristic parameters of rebar

	Diameter (mm)	f_y (MPa)	f_u (MPa)	Elongation (%)
HRB400	12	489	651	21
HPB300	6	453	536	24

Note: the f_y and f_u present yield strength and tensile strength of rebar, respectively.

with carbon fiber sheets outside the measuring area to avoid stress concentration before the tensile test, as shown in Figure 6. Then, the f_t was investigated. The deformation data were obtained by the extensometer, and the quasi-static loading rate was set to 0.1 mm·min^{-1}.

The thin slabs were used for testing the f_f in a 20 kN compression machine by changing the chuck based on the ASTM C 1609 M. The midspan deflection data were collected by linear variable displacement transducer (LVDT).

According to the Chinese code GB/T 50081-2019, the f_{cu}, f_c, and E_c of ECC were tested by a 1000 kN compression machine. The deformation data under the axial compression were collected using two LVDTs.

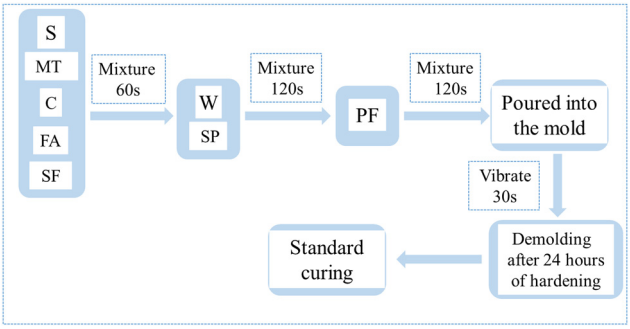

Figure 4: Specimen mixing process.

2.3.2 ECC pore structure testing

Industrial CT (MS-Voxe1450, Tianjin, China) was used to quantitatively evaluate the three-dimensional spatial pores distribution of ECC. In the scanning CT experiment, the operating voltage, current, and exposure time were 380 kV, 1.3 mA, and 0.5 s, respectively. The cube specimen was scanned continuously along the cross section to a depth of 0.5 mm, and every 20 mm along the height of the specimen. Finally, the 200 2D tomography CT images with 1,200 × 1,200 pixels resolution were acquired. The AVIZO 3D image processing software was used to perform the 3D reconstruction of pores by threshold segmentation.

The MacroMR12-150H-I NMR instrument was used to test the T_2 spectrum and pore fluid distribution of ECC. The magnetic field and frequency were selected at 0.5T and 50–60 Hz, respectively.

2.3.3 ECC micro-morphology testing

The specimen size was approximately 0.5 cm × 0.5 cm × 0.2 cm. Before gold spraying and vacuuming the sample, the prepared samples were pretreated by being placed in ethanol for 24 h and dried at 40°C for 24 h. Then, the micromorphology test was conducted using the EVO-10 SEM.

Table 5: Mix proportions (kg·m^{-3})

No.	Fine aggregates		Cementitious materials			W	SP	PF	Flow diameter (mm)	28 days f_{cu} (MPa)
	S	MT	C	FA	SF					
MT0	629	0	754.8	377.4	125.8	377	6.3	26	175	38.22
MT25	471.7	157.3	754.8	377.4	125.8	377	6.3	26	165	45.68
MT50	314.5	314.5	754.8	377.4	125.8	377	6.3	26	160	42.81
MT75	157.3	471.7	754.8	377.4	125.8	377	6.3	26	150	41.1
MT100	0	629	754.8	377.4	125.8	377	6.3	26	145	36.5

Nomenclature: using “MT25” as an example, MT denotes molybdenum tailing. The 25 denotes an MT replacement ratio of 25%.

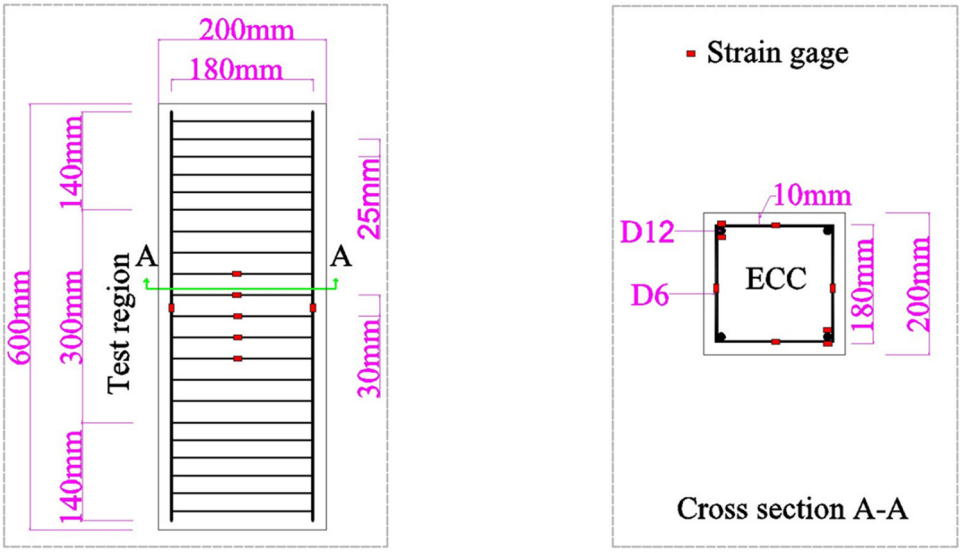

Figure 5: Dimensions of stub column: (a) elevation dimension and (b) cross-section dimension and strain gauge locations.

Table 6: Parameters of the column

No.	Length × width × thickness (mm)	Stirrup ratio of volume (%)	Stirrup spacing (mm)	MT replacement ratio (%)
CE-MT0	600 × 200 × 200	2.1	30	0
CE-MT25	600 × 200 × 200	2.1	30	25
CE-MT50	600 × 200 × 200	2.1	30	50
CE-MT75	600 × 200 × 200	2.1	30	75
CE-MT100	600 × 200 × 200	2.1	30	100

2.3.4 Stirrup-confined ECC stub column mechanical properties testing

The ECC square section stub column was loaded on a 5000 kN compression machine, as shown in Figure 7. A mixed loading method of force and displacement was used. At the initial stage, the loading rate of 100 kN·min^{-1} was selected to control loading. After the specimens reached the maximum compressive load, the loading rate of 0.3 mm·min^{-1} was selected to control loading. The axial deformation of the column was measured using two LVDTs laid on the side. The peak stress of the column (f_{cc}) was calculated by Eq. (1).

$$f_{cc} = \frac{N_u(\varepsilon_{cc}) - A_{cov}\sigma_{cov}(\varepsilon_{cc}) - A_s\sigma_s(\varepsilon_{cc})}{A - A_{cov} - A_s}, \quad (1)$$

where the A_{cov}, A_s, and A present the area of concrete cover, the cross-sectional area of longitudinal rebar, and the cross-sectional area of the specimen, respectively; the $N_u(\varepsilon_{cc})$, $\sigma_{cor}(\varepsilon_{cc})$, and $\sigma_s(\varepsilon_{cc})$ present the bearing capacity of the column, the stress of the concrete cover, and longitudinal rebar when the axial compressive strain of the column is ε_{cc}, respectively.

2.3.5 Environmental impact (EI) assessment

Based on the reliability and applicability of the life cycle assessment (LCA), this method is recommended to quantitatively assess the EI of a product [35,36]. According to ISO 14040 and ISO 14044 standards, to complete an assessment of the EI through the LCA, it is necessary to define the goal and functional units, create a life cycle inventory, and calculate the EI categories.

Thus, this study was devoted to investigating the EI (cradle-to-gate) of prepared ECC with different MT replacement ratios at first. The defined functional unit is 1 m^3 of ECC of a certain quality [37]. Then, the data relevant to the production of ECC from the life cycle inventory process and the LCA handbook were collected and calculated for the different EI categories.

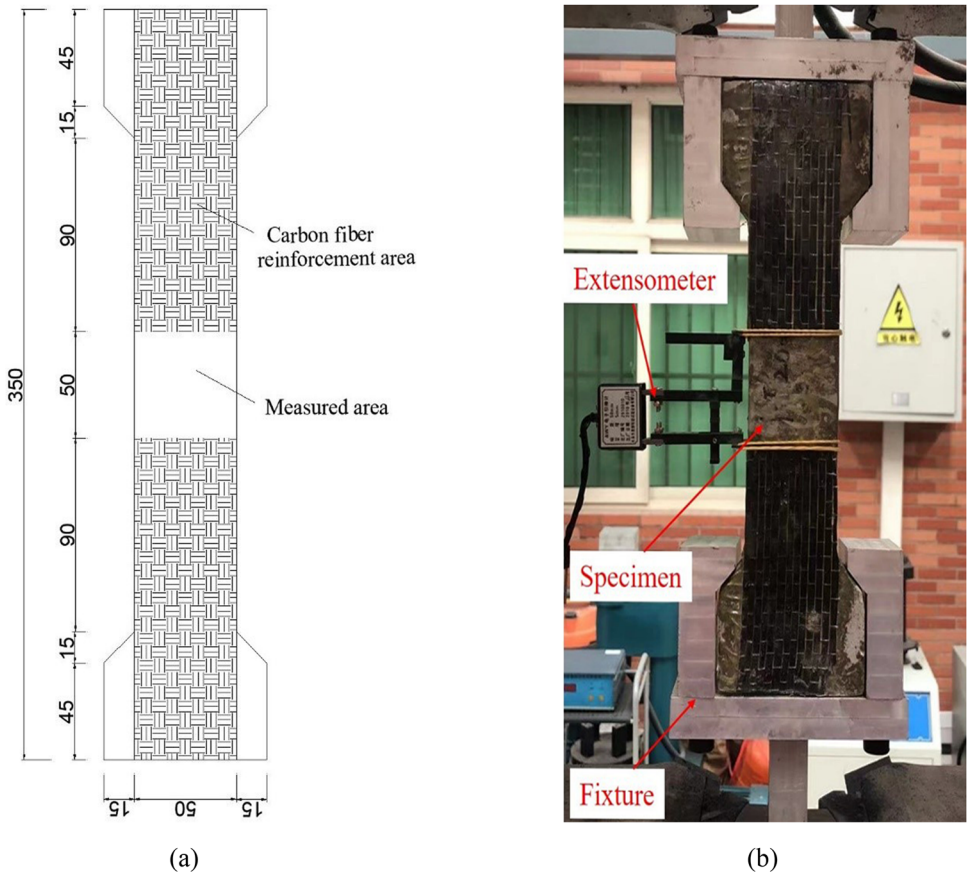

Figure 6: Uniaxial tension test: (a) specimen size and (b) test setup.

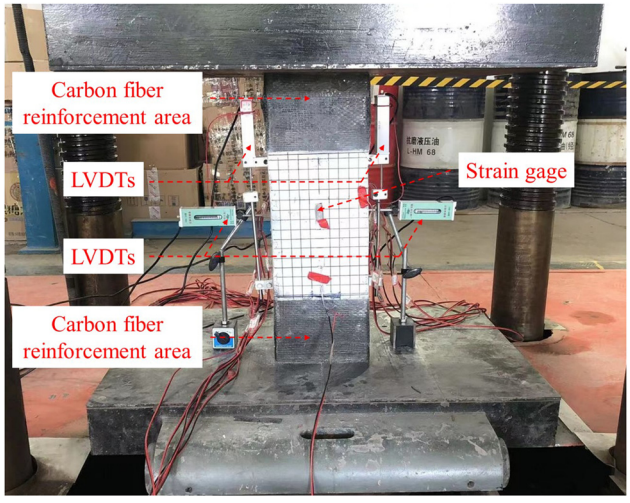

Figure 7: Compressive test setup.

The EI of the ECC was evaluated by five internationally recognized impact categories namely the photochemical ozone creation potential (POCP), acidification potential (AP), global warming potential (GWP), ozone depletion potential (ODP), and nitrification potential (NP) [38,39]. It should be noted that the EIs of MT and S during collection and transportation were not included in the life cycle analysis because both the MT plants and the sand plants are similar in distance to the city.

2.3.6 Cost assessment

The economic benefits of ECC with different MT replacement ratios were assessed by material costs.

3 Results and discussion

3.1 Uniaxial tension performance of ECC

3.1.1 Tensile stress–strain curves

The stress–strain curves of ECC under uniaxial tension are presented in Figure 8. Compared with MT0, the MT

incorporation did not change the shape of the stress–strain curve of the ECC, which still contains three stages. The elastic stage presents linear-elastic performance, and the tension stress is mainly resisted by the matrix. The strain-hardening stage presents that deformation increases significantly, but only a small increase in tensile stress. The strain-softening stage is mainly that the bonding stress between the matrix and fiber resists the tensile stress, and no new cracks are generated. The cracks generated in the second stage widen with the decrease of the bonding force and finally break with the main crack. By observing the strain-hardening stage, it can be found that the strain-hardening behaviors of MT25, MT50, and MT75 are more significant than that of MT0, and the ε_{tr} is more than 2%. Similarly, Huang *et al.* [40] reported ECC preparation using iron ore tailings also exhibits desirable strain-hardening behavior.

3.1.2 Tensile tests results

Table 7 lists the average values of test results including first cracking f_t, f_t, and tensile strain (ε_{tr}). It found that the incorporation of MT up to 75% is beneficial to enhancing the tensile properties of ECC, and incorporating 25% MT is the most significant improvement. The test results of three characteristic points of MT25 including first cracking f_t, f_t, and ε_{tr} increased by 22.69, 32.16, and 26.7%, respectively, compared with MT0. The improvement of tensile properties is mainly because the fine MT particles than that of S can effectively fill and refine the pores inside the matrix [41] and at the interface of PF and matrix so that the matrix density and bonding between the PF and the matrix will be increased, which can effectively consume energy during loading. Meanwhile, due to MT with more angular surfaces, this fact also facilitates the bonding between the PF and the matrix, increasing the tensile properties. A similar result is consistent with the previous study [42]. Unfortunately, when S is completely replaced by MT, the

Table 7: Tensile test results of ECC

No.	First cracking f_t (MPa)	f_t (MPa)	ε_{tr} (%)
MT0	2.52 (0.19)	3.46 (0.06)	1.89 (0.02)
MT25	3.26 (0.22)	5.10 (0.54)	2.58 (0.23)
MT50	3.15 (0.36)	4.55 (0.38)	2.34 (0.17)
MT75	2.77 (0.09)	4.01 (0.24)	2.09 (0.36)
MT100	1.98 (0.15)	2.81 (0.04)	1.62 (0.24)

Note: the values in parentheses represent the standard error.

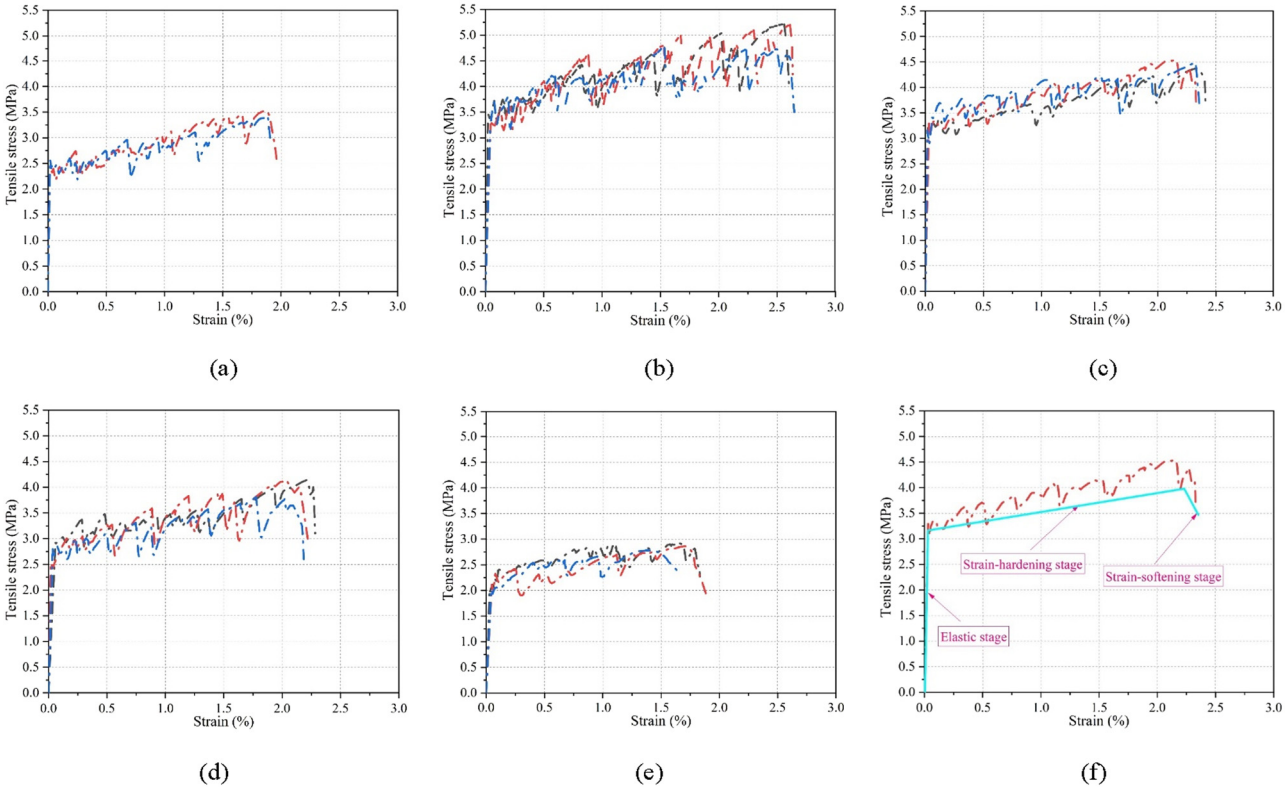

Figure 8: Stress–strain curve of ECC under uniaxial tension: (a) MT0, (b) MT25, (c) MT50, (d) MT75, (e) MT100 and (f) three-stages simplified model.

tensile properties of MT100 is deteriorated, especially at first cracking f_t, which decreased by 21.42%. The decrease in tensile properties is mainly due to poor gradation increases in the porosity, resulting in deterioration of the bonding between the matrix and PF. In addition, the amount of cement slurry attached to the MT per unit area is reduced, which weakens the bonding including between matrix and aggregate (matrix and PF). This is also confirmed in Sections 3.4 and 3.5. It can be observed from the above research results incorporating 25% MT could ensure high tensile properties, which further solidifies that incorporation of MT to prepare ECC is a promising clean production method.

3.2 Flexural performance of ECC

3.2.1 Load–deflection curves

Figure 9 presents the load–deflection curves of ECC under flexural load. Similar to the tensile stress–strain curve, the load–deflection curve also contains three parts (elastic part, deflection-hardening part, and descending softening part). The area covered by the load–deflection curve of ECC addition 25% MT is the largest, and the characteristic of deflection-hardening is obvious. But, as the MT replacement ratio increases, the area covered by the load–deflection curve and characteristic of deflection-hardening gradually deteriorated, especially at 100%, which is less than MT0.

3.2.2 Flexural tests results

Table 8 lists the test results of flexural properties. It was found that the first cracking deflection of ECC fluctuates without an obvious change in the law. The first cracking deflection of ECC incorporating 100% MT is the largest. This is because, when S is completely replaced by MT, the overall stiffness of the ECC decreases. The ultimate deflection of the ECC initially increased and then decreased as increasing MT replacement ratio, which is similar to the changing trend of the tensile test results. The ultimate deflection of ECC incorporating 25% MT has the most significant, which increased by 43.28%, compared with MT0. Similarly, MT25 has also the highest first cracking load and f_f, which increased by 19.43 and 19.79%, compared with MT0, respectively. This is mainly related to the high

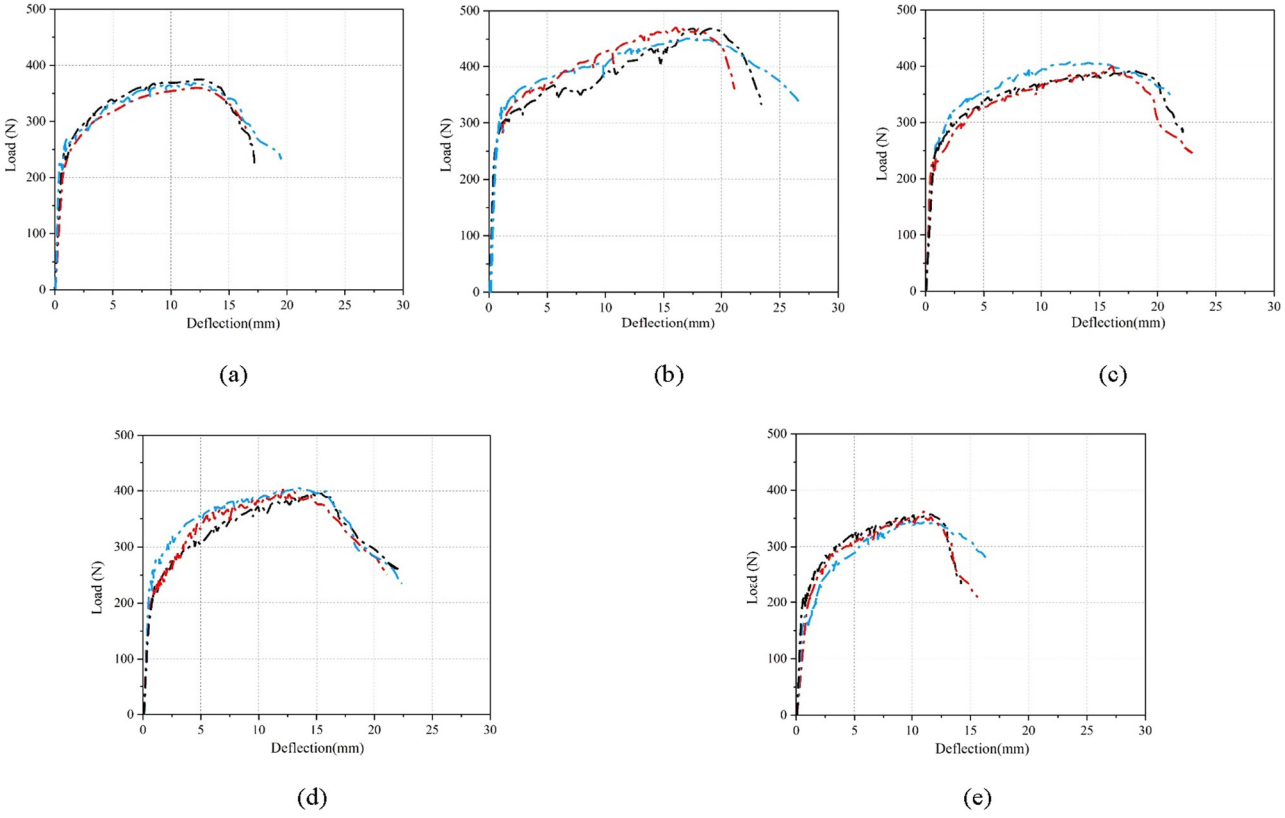

Figure 9: Load–deflection curve of ECC under flexural load: (a) MT0, (b) MT25, (c) MT50, (d) MT75, and (e) MT100.

Table 8: Flexural test results of ECC

No.	First cracking deflection (mm)	First cracking load (.)	Ultimate deflection (mm)	Ultimate load (N)	f_f (MPa)
MT0	0.61 (0.06)	210.36 (17.65)	12.66 (0.89)	376.94 (4.22)	7.09 (0.08)
MT25	0.59 (0.02)	251.24 (11.22)	18.14 (1.78)	473.09 (11.25)	8.84 (0.29)
MT50	0.63 (0.03)	215.18 (9.49)	16.13 (2.63)	395.48 (7.78)	7.39 (0.18)
MT75	0.56 (0.03)	206.23 (23.54)	13.08 (2.04)	401.12 (5.33)	7.57 (0.11)
MT100	0.73 (0.09)	186.59 (27.18)	11.11 (1.56)	343.06 (6.56)	6.41 (0.15)

Note: the values in parentheses represent the standard error.

compactness and the good interaction between the PF and the matrix of MT25. However, when the MT replacement ratio is 100%, the first cracking load, ultimate deflection, and f_f of ECC are deteriorated and smaller than that of MT0. Thus, ECC with 25–75% MT also has a favorable effect on the improvement of flexural properties.

3.2.3 Flexural toughness evaluation

Toughness under flexural stress is also an important indicator of material performance. At present, the evaluation methods of flexural toughness of composite materials mainly include JSCE-SF4, ASTM C1018, ASTM C 1609, RILEMT C162-TDF, and CECS 13-2009, which define and evaluate flexural toughness from different angles. However, of the many evaluation methods, the ASTM C1018 standard is an energy ratio method, which has relatively clear physical significance and is widely used. Based on the ASTM C1018 standard, this article uses toughness indexes to evaluate the toughness of ECC.

According to the load–deflection curve, the toughness index (I) can be calculated by the first crack deflection (δ_c) in a specimen and its corresponding energy (the area under the load–deflection curve), as shown in Eq. (2).

$$I_m = \frac{\int_0^{\frac{(m+1)\delta_c}{2}} P(\delta)\mathrm{d}\delta}{A_0},\ A_0 = \int_0^{\delta_c} P(\delta)\mathrm{d}\delta, \tag{2}$$

Table 9: Toughness indexes

No.	I_{10}	I_{30}	I_{50}	I_u
MT0	11.12 (0.56)	33.28 (2.19)		45.94 (3.16)
MT25	13.15 (1.62)	42.36 (3.06)	61.5 (4.78)	79.25 (5.26)
MT50	11.85 (1.1)	37.78 (2.77)	55.8 (2.93)	57.65 (3.03)
MT75	12.13 (1.56)	34.56 (2.5)		50.12 (2.89)
MT100	10.55 (0.88)	32.19 (1.98)		40.69 (3.12)

Note: the values in parentheses represent the standard error; I_u presents the toughness index under ultimate deflection.

where m presents the subscript of the I of different grades; the δ_c presents the first cracking deflection; the A_0 presents the area surrounded by the δ_c and the coordinate axis.

According to the literature [43], the ratios of the area under the corresponding curve of deformation under $5.5\delta_c$, $15.5\delta_c$, $25.5\delta_c$, and deformation under peak load δ_u divided by A_0 are taken as the toughness indexes, which were denoted I_{10}, I_{30}, I_{50}, and I_u, respectively. The calculated flexural toughness index of ECC is summarized in Table 9.

It can be observed that toughness indexes of ECC with different replacement ratios including I_{10}, I_{30}, I_{50}, and I_u were close to m, indicating that the toughness indexes of ECC under the flexural load satisfied the requirements. The toughness indexes of ECC incorporating 25–75% MT is higher than that of MT0, especially at 25%. In addition, It is worth noting that toughness indexes MT25 and MT50 have longer sequences. This is because of notably increasing bonding between the PF and the matrix due to the MT good "fill effect," and with more angular surfaces, the bond failure of the specimen will not occur prematurely during loading, showing a relatively obvious deflection hardening behavior, resulting in MT25 and MT50 have a remarkable flexural toughness. But up to 100% replacement ratio harms its toughness indexes.

3.3 Axial compressive performance of ECC

3.3.1 Compressive stress–strain curves

Figure 10 presents the stress–strain curves of ECC under axial compressive. Incorporating 25–75% MT could delay the decrease of post-peak f_c, especially at 25%. In addition, the $W_{0.85f_c}$ of MT25, MT50, and MT75 is higher than that of MT0, which indicates that the specimens could consume energy well. After the failure of all the specimens, there is still a significant residual f_c. Unfortunately, compared with MT0, the post-peak f_c of MT100 drops faster, and the residual f_c is smaller.

3.3.2 Axial compressive test results

Table 10 summarizes average values of f_c, axial compressive strain (ε_{cr}), E_c, $W_{0.85f_c}$, and residual f_c. It can be observed that when the replacement ratio of MT is less than 25%, the f_c of the ECC shows a change of increasing, while after exceeding 25%, the f_c of the ECC shows a gradually decreasing trend. For example, compared with MT0, the f_c of MT25, MT50, and MT75 increased by 17.7, 12.22, and 8.54%, respectively. Similarly, this is mainly attributed to the fine particle of MT being helpful to decrease the porosity, resulting in an increased f_c. Second, the "fill effect" of MT will result in the interfacial transition zone (ITZ) between matrix and aggregate being more dense and homogeneous and having no evident boundaries. Third, notably increasing bonding between the PF and the matrix due to MT with more angular surfaces, and "fill effect" restricts the lateral deformation of the test blocks and makes the whole test blocks be in a three-dimensional compression state, to improve the f_c. Similarly, the ε_{cr} of MT25, MT50, and MT75 increased by 11.06, 8.58, and 8.81%, respectively. However, the f_c and ε_{cr} of the MT100 decreased by 2.96 and 8.06%. This is mainly related to the fact that when the MT replacement ratio is 100%, the proportion of large-volume pores and the total porosity within the matrix increase. The bond strength between aggregates (matrix and PF) has also deteriorated.

It is worth noting that the E_c of ECC incorporating MT is higher than that of MT0. For example, the E_c of MT25, MT50, MT75, and MT100 increased by 4.8, 3.96, 2.24, and 1.8%, compared with MT0, respectively. A similar finding has been reported in past studies. Shettima *et al.* [44] also reported the fact that with the increase of iron ore tailings replacement level, the E_c was increased.

3.4 Pore characteristics of ECC

3.4.1 Three-dimensional spatial pore distribution from CT

Figure 11 shows the three-dimensional spatial pore distribution of ECC. When replacing S with 25–75% MT, the number of pores in MT25, MT50, and MT75 are lower than that of MT0. The best uniformity of pores space distribution inside MT25.

According to the different volumes of the pores, the pores can be divided into five ranges [45]. Figure 12 shows the percentage of the different pores volumes in ECC. It can be observed that the pores with volumes of 0–0.1 mm^3 are

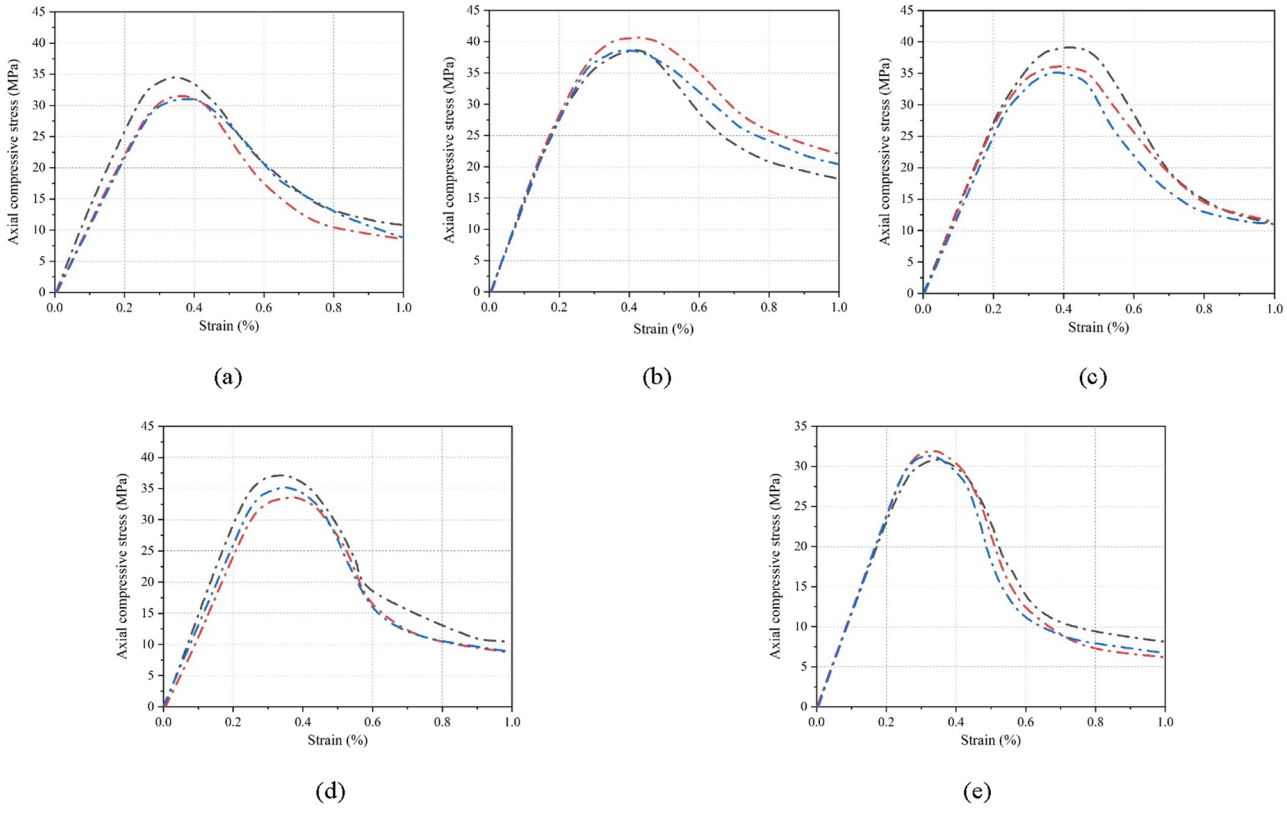

Figure 10: Stress–strain curve of ECC under axial compression: (a) MT0, (b) MT25, (c) MT50, (d) MT75, and (e) MT100.

Table 10: Axial compressive test results of ECC

No.	f_c (MPa)	ε_{cr} (%)	E_c (GPa)	$W_{0.85f_c}$	Residual f_c (MPa)
MT0	32.32 (0.28)	0.362 (0.17)	21.8 (0.19)	121.6 (0.21)	9.45 (0.33)
MT25	39.28 (0.09)	0.407 (0.20)	22.9 (0.02)	146.6 (0.34)	20.19 (0.46)
MT50	36.82 (0.11)	0.396 (0.08)	22.7 (0.07)	135.9 (0.28)	11.23 (0.19)
MT75	35.34 (0.33)	0.397 (0.53)	22.3 (0.31)	133.2 (0.17)	11.67 (0.58)
MT100	31.39 (0.04)	0.335 (0.28)	22.2 (0.09)	93.8 (0.12)	6.96 (0.29)

Note: the values in parentheses represent the standard error; $W_{0.85f_c}$ is the area enclosed by stress–strain curves under axial compressive from the origin to the f_c dropping to 85%.

the most widely distributed. When S is completely replaced by MT, the pore volumes of MT100 gradually increase. The proportion of the pores with volumes 0.01–0.05, 0.05–0.1, 0.1–0.5, and >0.5 mm^3 are higher than that of others, especially volumes >0.5 mm^3.

3.4.2 T2 spectrum and pore fluid distribution from NMR

Figure 13(a) shows the pore structure of ECC and that each T_2 spectrum curve includes the three peaks. Compared with the second and third peaks, the intensity of the first peak of the T_2 spectrum curve is significant, indicating that the internal pores of the ECC are mainly micro-pores. Figure 13(b) found that when replacing S with 25–75% MT, the total porosity of MT25, MT50, and MT75 are reduced by 33.1, 21.15, and 6.18%, respectively, indicating that incorporating MT could effectively reduce the internal pores, especially at 25%, which confirms the "filling effect" of MT when incorporating a less than 75% MT. In addition, this finding explains one of the reasons from a mesoscopic point of view why the mechanical properties of MT25 are better than that of other groups. Unfortunately, the total porosity of MT100 with a 100% MT replacement ratio increases more than that of MT0. This indicates that the complete replacement of S by MT deteriorates the matrix pore structure.

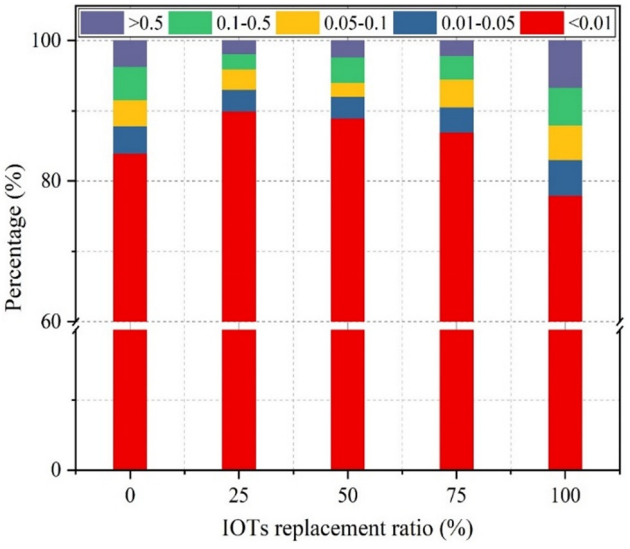

Figure 12: Percentage of different volume pores.

It is well known that pore structure has a direct effect on f_{cu} development. The concrete f_{cu} – porosity (P) model has been established by some scholars. Figure 14 shows the fitted results of the three models proposed in the literature [46] including models Hasselman proposed, Schiller proposed and Ryshkewitch proposed for f_{cu} – P, respectively. It can be observed that the increase of porosity results in the degradation of f_{cu}.

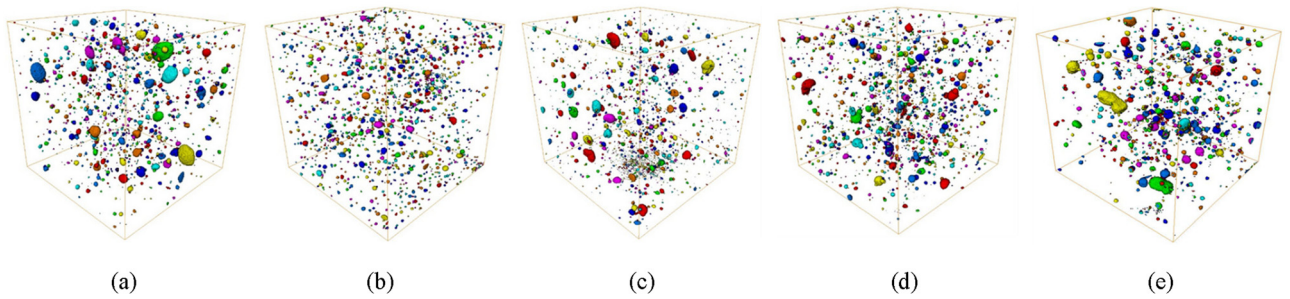

Figure 11: Three-dimensional spatial pores distribution: (a) MT0, (b) MT25, (c) MT50, (d) MT75, and (e) MT100.

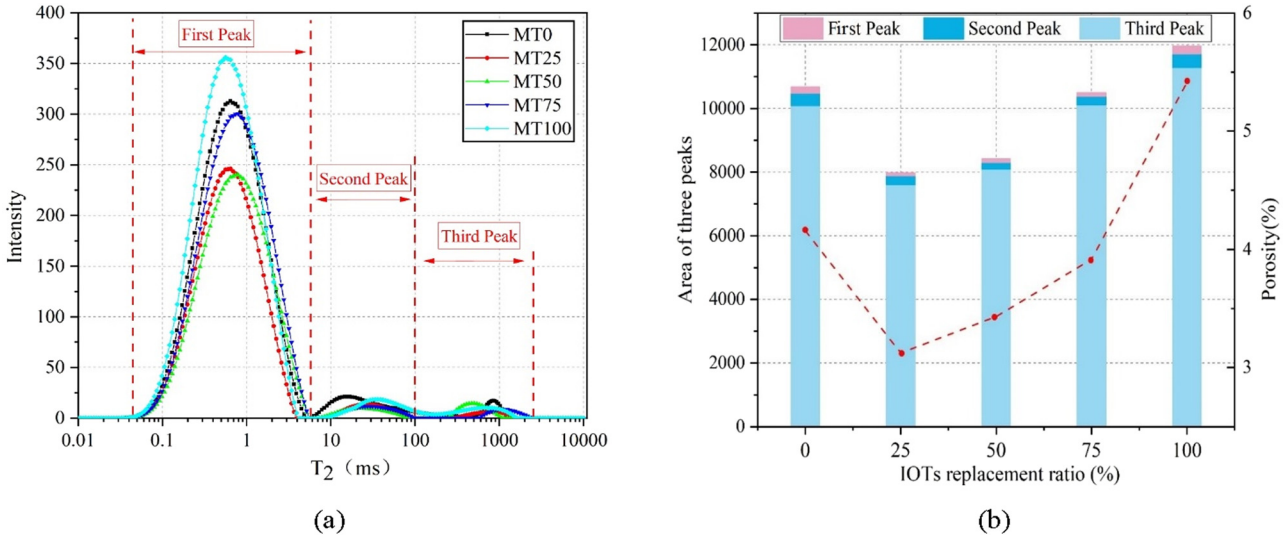

Figure 13: Pore structure of ECC with different MT replacement ratios. (a) T2 spectrum curve and (b) pore percentage.

Table 11 lists the errors between the calculation results of each model and the test results. The calculation results of the model proposed by Hasselman are lower, compared to the test results. However, the errors between the calculation results obtained by the model Schiller proposed and the test results are the smallest, which shows a good application.

3.5 Microstructure of ECC from SEM

Figure 15 shows the microstructure of ECC. Figure 15(a) shows that compared with MT0, the number of pores and connected pores inside the MT25, MT50, and MT75 is reduced, and the compactness of the microstructure of three is in the following order from high to low: MT25 > MT50 > MT75. However, when S is completely replaced by MT, the number of connected pores and pores inside the MT100 significantly increases, and the density of the matrix is relatively loose, compared with MT0.

The ITZ between the matrix and aggregate is shown in Figure 15(b). It is worth noting that as the MT replacement ratio increases, the ITZ gaps increase gradually. Compared with MT0, the ITZ gaps of the MT25, MT50, and MT75 are relatively small, especially MT25, which ITZ is well developed, and there are no obvious boundaries. Unfortunately, the ITZ gaps of MT100 are larger than that of MT0. Figure 15(c) shows the bonding interface between PF and the matrix. Similarly, it can be observed that incorporating up to 75% MT has a positive effect on the bonding interface between PF and the matrix. Under the 25% MT replacement ratio, PF is the best embedded in the matrix. However, under the 100% MT replacement ratio, the bonding interface MT100 is smaller than that of MT0. The SEM analysis results explain the high strength of MT25 from the microscopic points of view. It can be observed from Figure 15(d) found that the ultimate bonding failure occurs between fiber and matrix under load.

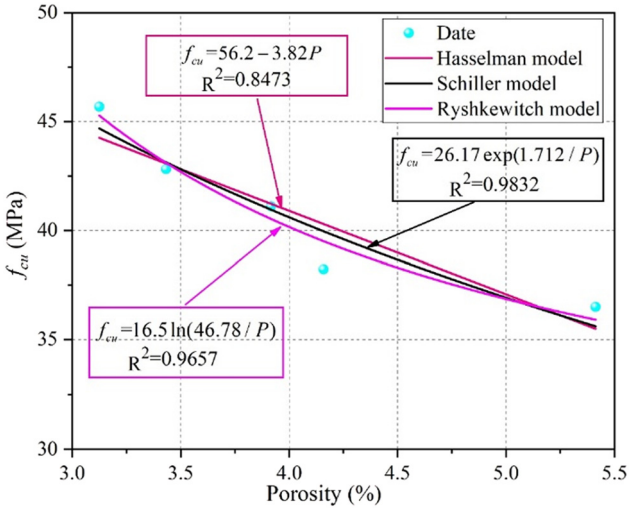

Figure 14: Relationship between f_{cu} and porosity.

Table 11: The errors between the calculation results of each model and test results

Model	Hasselman model	Schiller model	Ryshkewitch model
Error range (%)	−0.6 to −11.36	−3.55 to 1.48	−4.5 to 2.49

3.6 Axial compressive performance of stirrup-confined ECC stub column

3.6.1 Failure phenomenon

Figure 16 presents the failure patterns of columns. Due to the inhibition of PF, all the columns' surfaces, except for many intricate cracks, did not fall off. With the MT replacement ratio increasing, the destruction of the columns seems to be more serious. For example, the width of cracks in the CE-MT25, CE-MT50, and CE-M T75 gradually increases, but the width of the crack is still smaller than that of CE-MT0. However, the width and number of cracks in the CE-MT100 increased significantly, compared with CE-MT0.

3.6.2 Axial force–strain relationship curve

Figure 17 presents the axial force–axial strain curve of the column. The column cracking, the rising segment of the curve, is not different by increasing the MT replacement ratio. Meanwhile, the initial stiffness of the column incorporating up to 75% MT exhibited insignificant differences. However, the initial stiffness of the column with 100% MT is reduced, which is consistent with the reduction in the f_c of ECC. After reaching the peak stress, the curve enters the descending section. It can be observed that the influence of the MT replacement ratio on the descending segment of the curve is significantly greater than that of the rising segment. The descending section of the curve of the

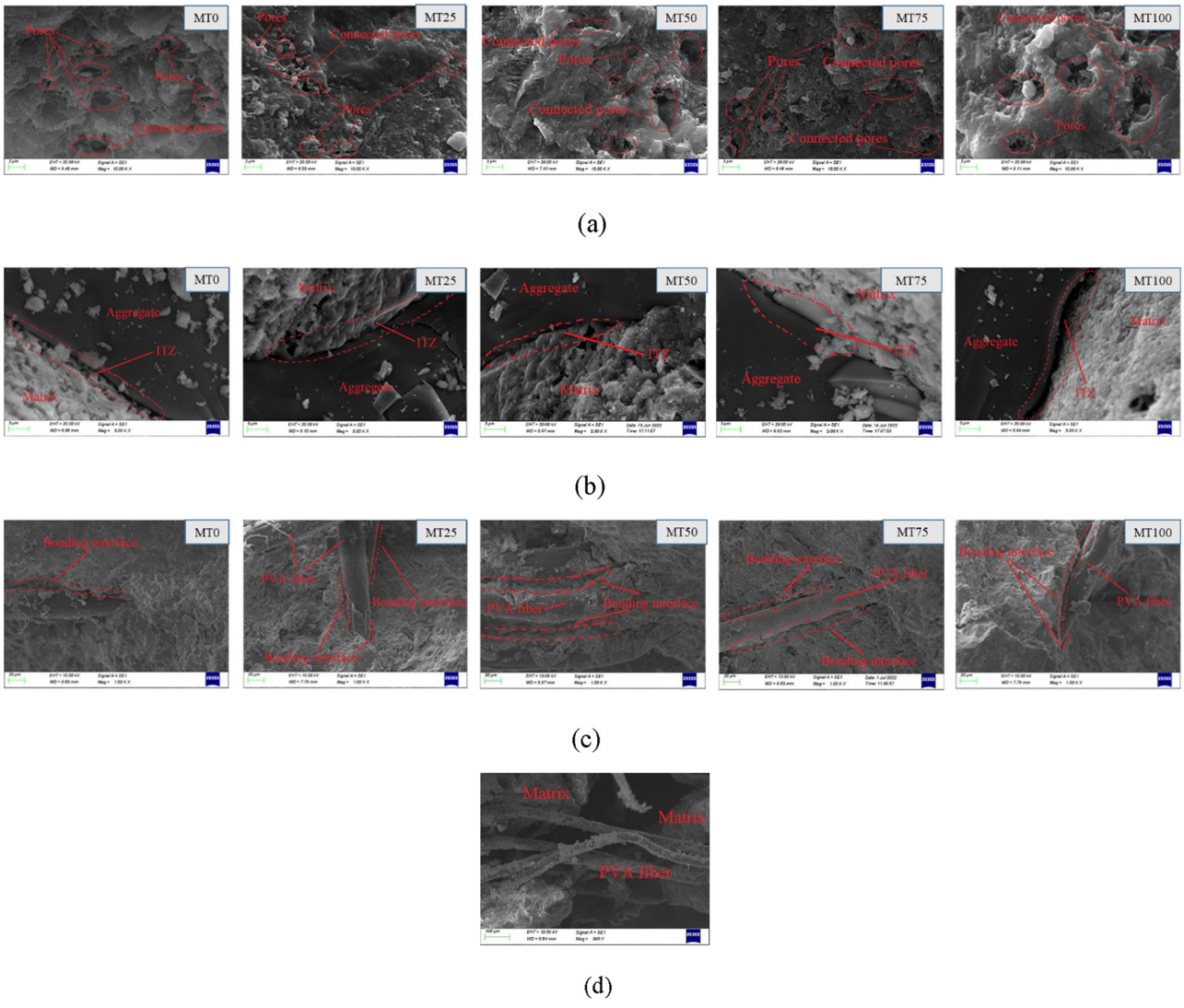

Figure 15: Microstructure of ECC: (a) effect of MT replacement ratio on matrix, (b) effect of MT replacement ratio on ITZ, (c) effect of MT replacement ratio on the bonding interface, and (d) debonding between PF and matrix.

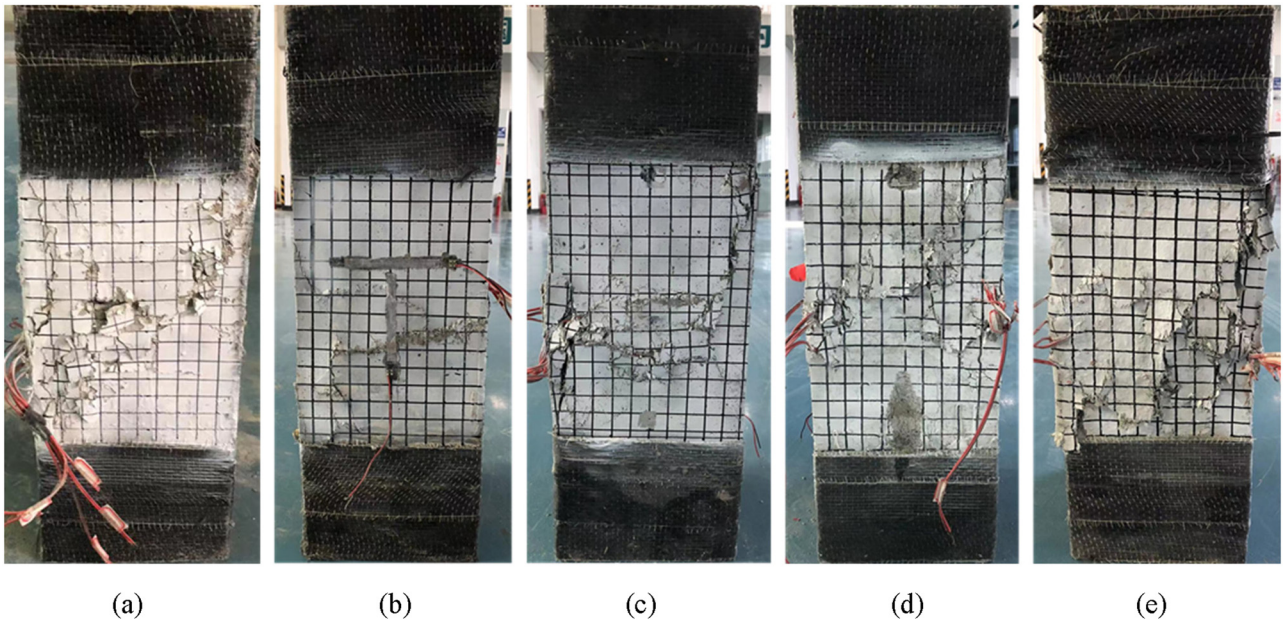

Figure 16: Failure patterns of columns: (a) CE-MT0, (b) CE-MT25, (c) CE-MT50, (d) CE-MT75, and (e) CE-MT100.

column with the higher ultimate bearing capacity is steeper because the stirrups play the role of passive restraint later. However, the descending section of the column with the lower ultimate bearing capacity is flat. This indicates that for ECC columns with low strength, the stirrup can give full play to its restraint effect.

3.6.3 Axial compressive test results

Table 12 summarizes the main test results including N_u, f_{cc}, and ε_{cc} of the column under axial compression. When the MT replacement ratio increases to 75%, both the f_{cc} and ε_{cc} of the column increase. For example, compared with CE-MT0, when the MT replacement ratio is 25, 50, and 75%, respectively, the f_{cc} of the column increased by 9.75, 6.39, and 1.33%, and its ε_{cc} increased by 14.94, 9.76, and 3.89%. Furthermore, it is noteworthy that the residual bearing capacity of CE-MT25, CE-MT50, and CE-MT75 is relatively high after the column failure. This is mainly attributed to the combined effect of the lateral restraint of the stirrup and the bridging restraint of the fibers.

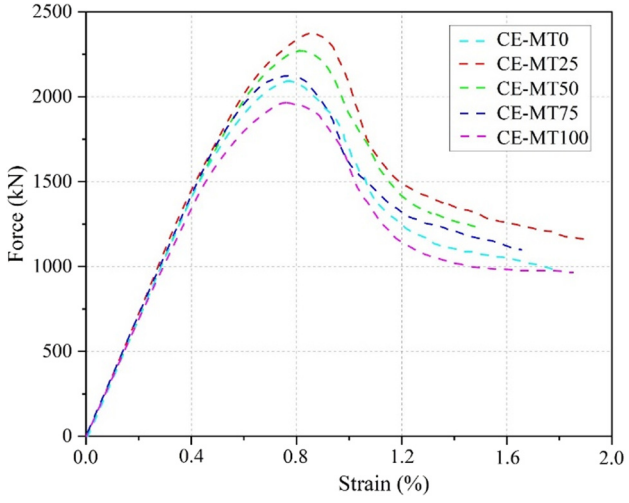

Figure 17: Representative axial force–strain curve.

3.7 EI of ECC

According to the literature and the material's environmental statements [47–51], the life cycle inventory analysis of producing each ECC's raw materials is summarized in Table 13. Based on the fact that MT is an industrial by-product and the discharge meets the relevant standards, the emissions associated with MT production are not

Table 12: Axial compressive test results of the columns

No.	N_u (kN)	f_{cc} (MPa)	ε_{cc} (%)
CE-MT0	2116.48	54.33	0.74
CE-MT25	2377.34	60.2	0.87
CE-MT50	2274.34	58.04	0.82
CE-MT75	2125.78	55.06	0.77
CE-MT100	1964.43	50.25	0.73

where N_u is the ultimate bearing capacity of the column under compression.

Table 13: LCA data of ECC raw materials

	C	FA	SF	S	SP	MT
GWP (kg CO_2·kg^{-1})	0.691	0.35	1.2	1.02×10^{-2}	0.944	0
POCP (kg R11·kg^{-1})	1.0×10^{-4}	9.34×10^{-5}	1.09×10^{-4}	2.58×10^{-6}	5.58×10^{-4}	0
ODP (kg C_2H_4·kg^{-1})	1.50×10^{-8}	6.67×10^{-9}	4.59×10^{-6}	2.10×10^{-9}	3.29×10^{-8}	0
NP (kg PO_4·kg^{-1})	1.2×10^{-5}	1.52×10^{-4}	5.48×10^{-4}	3.00×10^{-6}	5.97×10^{-3}	0
AP (kg SO_2·kg^{-1})	8.30×10^{-4}	2.67×10^{-3}	7.07×10^{-3}	7.54×10^{-5}	1.19×10^{-2}	0

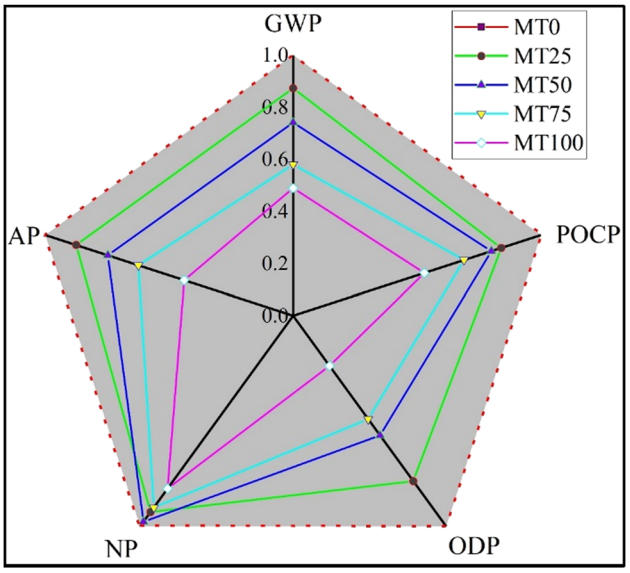

Figure 18: EI of ECC with different MT replacement ratios.

considered. Moreover, the PF is also not considered due to the uniform amount of fiber in all mixtures in the calculation.

To quantitatively evaluate the EI of the ECC with different replacement ratios, the EI of producing 1 m^3 of ECC is calculated, and obtained results are normalized based on MT0, as shown in Figure 18. It is clear that the environmental overload gradually decreases and the multi-deformation line of IOTCC is closest to the origin with increasing the replacement ratio of MT. For example, the GWP, POCP, ODP, NP, and AP of the MT25 decreased by 12.7, 7.54, 21.54, 0.7, and 12.39%, respectively, compared to the MT0. Therefore, the above results concluded that using MT as aggregate to prepare ECC is an ideal clean production method.

3.8 Cost assessment

The total cost of 1 m^3 of ECC is listed in Table 14. The cost of each material comes from the price of local suppliers in Xi'an, China. MT is provided free of charge as waste [52,53]. It can be seen from Table 14 that the total cost of ECC decreases gradually with the increase of the MT replacement ratio. The incorporation of MT is helpful to reduce ECC costs and further promotes the sustainable application of MT as eco-friendly material in construction products.

4 Conclusions

A comprehensive evaluation of the ECC with MT as aggregate was conducted, which mainly included the mechanical properties, pore distribution, and microstructure. Conclusions were obtained as follows:

1) The chemical composition, physical properties, and radioactivity of MT confirmed the feasibility to prepare ECC. As the MT replacement ratio increases, the compressive, tensile, and flexural properties of ECC initially increased and then decreased. The ECC with 25% MT exhibited the best

Table 14: Material cost (1 m^3)

No.	Material cost ($ per kg)								Total cost per m^3
	C	FA	SF	S	PF	MT	W	SP	
	0.070	0.020	0.310	0.041	40.15	0.000	0.001	0.896	
MT0	48.440	7.548	58.497	22.624	1043.9	0.000	0.377	5.071	1186.458
MT25	48.440	7.548	58.497	16.968	1043.9	0.000	0.377	5.098	1180.929
MT50	48.440	7.548	58.497	11.312	1043.9	0.000	0.377	5.080	1175.155
MT75	48.440	7.548	58.497	5.656	1043.9	0.000	0.377	5.116	1169.535
MT100	48.440	7.548	58.497	0.000	1043.9	0.000	0.377	5.161	1163.23

mechanical properties. The f_t of MT25 increased 32.16%, compared with only S as aggregate.

2) The CT and NMR results found that when the MT replacement ratio was less than 75%, the total porosity of ECC was reduced and the number and volume of spatially distributed pores were also reduced, compared with MT0. The ECC with 25% MT exhibits a better pore structure.
3) SEM micro morphology results indicated that ECC with 25% MT exhibited good ITZ and bonding interface between PF and matrix. The microstructure of ECC is relatively dense.
4) The axial compression results of the stirrup-confined ECC stub column indicated that the f_{cc}, ε_{cc}, and residual N_u of the column were improved by incorporating up to 75% MT. The stirrup-confined ECC stub column with 25% MT can ensure better mechanical properties.
5) Based on the assessment results of EI and cost, the replacement of S by MT for ECC application reduced the production EI and cost of ECC, especially with a higher replacement ratio, which further solidifies the argument that the incorporation of MT to prepare ECC is a promising method.

It should be pointed out that the MT used in this article is from a specific location (Shaanxi Province, China). There are differences in the MT produced in different locations (crystal composition, micromorphology, crushing index, particle size, *etc.*). Therefore, some of the conclusions obtained in this study may be different for ECC prepared using MT from other locations. In future research, the ECC prepared by MT from different locations should be systematically studied to gain a more in-depth understanding of this environment-friendly material. In addition, further studies on structural members (beams, joints, and walls) are conducted. The successful application of industrial byproduct MT as eco-friendly materials will further promote the sustainable development of the construction industry.

Acknowledgments: The authors would like to acknowledge the financial support.

Funding information: This work was supported by the Project on Key Research and Development of Shaanxi, China (No. 2021SF-521, No. 2022SF-375), Natural Science Foundation of Shaanxi, China (No. 2021JQ-844), Natural Science Basic Research Program of Shaanxi (Program No. 2022JQ-497), and The Natural Science Foundation of Shaanxi Province (2021JM-165,2021JM-170).

Author contributions: All authors have accepted responsibility for the entire content of this manuscript and approved its submission.

Conflict of interest: The authors state no conflict of interest.

References

[1] Xu, L. Y., B. T. Huang, V. C. Li, and J. G. Dai. High-strength high-ductility engineered/strain-hardening cementitious composites (ECC/SHCC) incorporating geopolymer fine aggregates. *Cement and Concrete Composites*, Vol. 125, 2022, id. 125.

[2] Xu, L. Y., B. T. Huang, J. C. Lao, J. Yao, V. C. Li, and J. G. Dai. Tensile over-saturated cracking of ultra-high-strength engineered cementitious composites (UHS-ECC) with artificial geopolymer aggregates. *Cement and Concrete Composites*, Vol. 136, 2023, id. 136.

[3] Huang, B. T., J. X. Zhu, K. F. Weng, V. C. Li, and J. G. Dai. Ultra-high-strength engineered/strain-hardening cementitious composites (ECC/SHCC): Material design and effect of fiber hybridization. *Cement and Concrete Composites*, Vol. 129, 2022, id. 129.

[4] Adesina, A. and S. Das. Mechanical performance of engineered cementitious composite incorporating glass as aggregates - ScienceDirect. *Journal of Cleaner Production*, Vol. 260, 2020, id. 121113.

[5] Guan, X., Y. Li, T. Liu, C. Zhang, H. Li, and J. Ou. An economical ultra-high ductile engineered cementitious composite with large amount of coarse river sand. *Construction and Building Materials*, Vol. 201, 2019, pp. 461–472.

[6] Zhang, Z. and Q. Zhang. Matrix Tailoring of engineered cementitious composites (ECC) with non-oil-coated, low tensile strength PVA fiber. *Construction and Building Materials*, Vol. 161, No. FEB.10, 2018, pp. 420–431.

[7] Xu, L. Y., B. T. Huang, Q. Lan-Ping, and J. G. Dai. Enhancing long-term tensile performance of engineered cementitious composites (ECC) using sustainable artificial geopolymer aggregates. *Cement and Concrete Composites*, Vol. 133, 2022, id. 104676.

[8] Xu, L. Y., B. T. Huang, J. C. Lao, and J. G. Dai. Tailoring strain-hardening behavior of high-strength engineered cementitious composites (ECC) using hybrid silica sand and artificial geopolymer aggregates. *Materialsand Design*, Vol. 220, 2022, id. 110876.

[9] Zhang, Z. G., H. Ma, and S. Z. Qian. Investigation on properties of ECC incorporating crumb rubber of different sizes. *Journal of Cleaner Production*, Vol. 13, No. 5, 2015, pp. 241–251.

[10] Li, J. and E. H. Yang. Macroscopic and microstructural properties of engineered cementitious composites incorporating recycled concrete fines. *Cement and Concrete Composites*, Vol. 78, 2017, pp. 33–42.

[11] Huang, X., R. Ranade, W. Ni, and V. C. Li. Development of green engineered cementitious composites using iron ore tailings as aggregates. *Construction and Building Materials*, Vol. 44, 2013, pp. 757–764.

[12] Turk, K. and S. Demirhan. The mechanical properties of engineered cementitious composites containing limestone powder replaced by microsilica sand. *Canadian Journal of Civil Engineering*, Vol. 40, No. 2, 2013, pp. 151–157.

[13] Siddique, S. and J. G. Jang. Assessment of molybdenum mine tailings as filler in cement mortar. *Journal of Building Engineering*, Vol. 31, 2020, id. 101322.

[14] Kinnunen, P., A. Ismailov, S. Solismaa, H. Sreenivasan, M. L. Räisänen, E. Levänen, et al. Recycling mine tailings in chemically

bonded ceramics – A review. *Journal of Cleaner Production*, Vol. 174, 2018, pp. 634–649.
[15] Dong, K., F. Xie, W. Wang, Y. Chang, D. Lu, X. Gu, et al. The detoxification and utilization of cyanide tailings: A critical review - ScienceDirect. *Journal of Cleaner Production*, Vol. 302, 2021, id. 126946.
[16] Quan, X. Y., S. L. Wang, K. N. Liu, J. Xu, N. Zhao, and B. Liu Influence of molybdenum tailings by-products as fine aggregates on mechanical properties and microstructure of concrete. *Journal of Building Engineering*, Vol. 54, 2022, id. 104677.
[17] Fontes, W. C., J. C. Mendes, S. N. Da Silva, and R. A. Peixoto. Mortars for laying and coating produced with iron ore tailings from tailing dams. *Construction & Building Materials*, Vol. 112, 2016, pp. 995–988.
[18] Osinubi, K. J., P. Yohanna, and A. O. Eberemu. Cement modification of tropical black clay using iron ore tailings as admixture. *Transportation Geotechnics*, Vol. 5, 2015, pp. 35–49.
[19] Bian, Z., X. Miao, S. Lei, S. E. Chen, W. Wang, and S. Struthers. The Challenges of Reusing Mining and Mineral-Processing Wastes. *Science*, Vol. 337, No. 6095, 2012, pp. 702–703.
[20] Davila, R. B., M. Fontes, A. A. Pacheco, and M. Ferreira. Heavy metals in iron ore tailings and floodplain soils affected by the Samarco dam collapse in Brazil. *Science of the Total Environment*, Vol. 709, 2019, id. 136151.
[21] Han, F., L. Li, S. Song, and J. Liu. Early-age hydration characteristics of composite binder containing iron tailing powder. *Powder Technology*, Vol. 315, 2017, pp. 315–331.
[22] Kim, M. J. and Y. Jung. Vertical distribution and mobility of arsenic and heavy metals in and around mine tailings of an abandoned mine. *Environmental Letters*, Vol. 39, No. 1, 2004, pp. 203–222.
[23] Sun, Y., R. Yu, S. Wang, Y. Zhou, M. Zeng, F. Hu, et al. Development of a novel eco-efficient LC2 conceptual cement based ultra-high performance concrete (UHPC) incorporating limestone powder and calcined clay tailings: Design and performances - ScienceDirect. *Journal of Cleaner Production*, Vol. 315, 2021, id. 128236.
[24] Zhang, C. and S. Li. Utilization of iron ore tailing for the synthesis of zeolite A by hydrothermal method. *Journal of Material Cycles and Waste Management*, Vol. 20, 2018, pp. 1605–1614.
[25] Shi, J., F. He, C. Ye, L. Hu, J. Xie, H. Yang, et al. Preparation and characterization of CaO–Al2O3–SiO2 glass-ceramics from molybdenum tailings. *Materials Chemistry and Physics*, Vol. 57–64, No. 197, 2017, pp. 57–64.
[26] Wang, X. L., J. M. Wang, and Z. J. Ma. Experimental research on recovery of phlogopite from molybdenum tailings. *Bulletin of the Chinese Ceramic Society*, Vol. 1010, 2014, pp. 1609–1612.
[27] Jiangang, F., C. Kaida, W. Hui, G. Chao, and L. Wei. Recovering molybdenite from ultrafine waste tailings by oil agglomerate flotation - ScienceDirect. *Minerals Engineering*, Vol. 39, No. 1, 2012, pp. 133–139.
[28] Antonelli, P. M., L. H. Fraser, W. C. Gardner, K. J. Broersma, and M. E. Phillips. Long term carbon sequestration potential of biosolids-amended copper and molybdenum mine tailings following mine site reclamation. *Ecological Engineering the Journal of Ecotechnology*, Vol. 117, 2018, pp. 38–49.
[29] Jung, M. Y. and C. J. G. Jeong. Recycling of tailings from Korea Molybdenum Corporation as admixture for high-fluidity concrete. *Environmental Geochemistry & Health*, Vol. 33, Suppl 1, 2011, pp. 113–119.
[30] Gao, S. and S. B. Kang. Sustainable applications for utilizing molybdenum tailings in concrete. *Journal of Cleaner Production*, Vol. 266, 2020, id. 122020.
[31] Gao, S. and L. Guo. Mechanical properties of circular thin-tubed molybdenum tailing concrete stubs. *Construction and Building Materials*, Vol. 268, 2020, id. 121215.
[32] Siddique, S. and J. G. Jang. Assessment of molybdenum mine tailings as filler in cement mortar. *Journal of Building Engineering*, Vol. 31, 2020, id. 101322.
[33] Yu, R., E. Dong, Z. Shui, D. Qian, D. Fan, J. Wang, et al. Advanced utilization of molybdenum tailings in producing ultra high-performance composites based on a green activation strategy. *Construction and Building Materials*, Vol. 330, 2022, id. 127272.
[34] Li, V. C. and C. K. Y. Leung. Steady-state and multiple cracking of short random fiber composites. *Journal of Engineering Mechanics*, Vol. 118, No. 11, 1992, pp. 2246–2264.
[35] Kurda, R., J. D. Brito, and J. D. Silvestre. A comparative study of the mechanical and life cycle assessment of high-content fly ash and recycled aggregates concrete. *Journal of Building Engineering*, Vol. 29, 2020, id. 101173.
[36] Chen, X., H. Wang, H. Najm, G. Venkiteela, and J. Hencken. Evaluating engineering properties and environmental impact of pervious concrete with fly ash and slag. *Journal of Cleaner Production*, Vol. 237, 2019, id. 117714.
[37] Han, Y., Z. Yang, T. Ding, Xiao J. Environmental and economic assessment on 3D printed buildings with recycled concrete. *Journal of Cleaner Production*, Vol. 278, No. 2, 2020, id. 123884.
[38] Wang, X., R. Yu, Z. Shui, Z. Zhao, Q. Song, B. Yang, et al. Development of a novel cleaner construction product: Ultra-high performance concrete incorporating lead-zinc tailings. *Journal of Cleaner Production*, Vol. 196, No. pt.1-862, 2018, pp. 172–182.
[39] Russell, A. J. Handbook on life cycle assessment: Operational guide to the ISO standards. *Journal of Cleaner Production*, B. Guinée Jeroen, Ed., Kluwer Academic Publishers, Dordrecht, 2005, Vol. 13, No. 13–14, pp. 1359.
[40] Huang, X., R. Ranade, Q. Zhang, W. Ni, and V. C. Li. Mechanical and thermal properties of green lightweight engineered cementitious composites. *Construction and Building Materials*, Vol. 48, No. nov., 2013, pp. 954–960.
[41] Na, Z. A., B. Bt, and B. Xl. Cementitious activity of iron ore tailing and its utilization in cementitious materials, bricks and concrete. *Construction and Building Materials*, Vol. 288, 2021, id. 123022.
[42] Zhou, A., H. Wei, T. Liu, D. Zou, Y. Li, and R. Qin. Interfacial technology for enhancement in steel fiber reinforced cementitious composite from nano to macroscale. *Nanotechnology Reviews*, Vol. 10, No. 1, 2021, pp. 636–652.
[43] Lin, C., S. Wang, M. Chen, and Y. Lu. Experimental study on the mechanical properties of different fiber-reinforced seawater sea-sand engineered cementitious composites. *Construction and Building Materials*, Vol. 304, 2021, id. 124562.
[44] Shettima, A. U., M. W. Hussin, Y. Ahmad, and J. Mirza. Evaluation of iron ore tailings as replacement for fine aggregate in concrete. *Construction & Building Materials*, Vol. 120, No. sep. 1, 2016, pp. 72–79.
[45] Liu, F., T. Zhang, T. Luo, M. Zhou, K. Zhang, and W. Ma. Study on the deterioration of concrete under dry-wet cycle and sulfate attack. *Materials*, Vol. 13, No. 18, 2020, id. 4095.
[46] Liu, L., Z. He, X. Cai, and S. Fu. Application oflow-field NMR to the pore structure of concrete. *Applied Magnetic Resonance*, Vol. 2020, No. 2, 2020, pp. 1–17.
[47] Marinkovi, S. B. Life cycle assessment (LCA) aspects of concrete. *Eco-Efficient Concrete*, 2013, pp. 45–80.

[48] Habert, G., J. Lacaillerie, and N. Roussel. An environmental evaluation of geopolymer based concrete production: reviewing current research trends. *Journal of Cleaner Production*, Vol. 19, No. 11, 2011, pp. 1229–1238.
[49] Caldas, L. R., M. H. Da Gloria, F. Pittau, V. M. Andreola, G. Habert, and R. D. Toledo Filho. Environmental impact assessment of wood bio-concretes: Evaluation of the influence of different supplementary cementitious materials - ScienceDirect. *Construction and Building Materials*, Vol. 268, 2021, id. 121146.
[50] Vargas, F., M. Lopez, and L. Rigamonti. Environmental impacts evaluation of treated copper tailings as supplementary cementitious materials. *Resources Conservation and Recycling*, Vol. 160, 2020, id. 104890.
[51] Muller, H. S., M. Haist, and M. Vogel. Assessment of the sustainability potential of concrete and concrete structures considering their environmental impact, performance and lifetime. *Construction and Building Materials*, Vol. 67, 2014, pp. 321–337.
[52] Gao, S. and S. B. Kang. Sustainable applications for utilizing molybdenum tailings in concrete. *Journal of Cleaner Production*, Vol. 266, 2020, id. 122020.
[53] Quan, X., S. Wang, J. Li, J. Luo, K. Liu, J. Xu, et al. Utilization of molybdenum tailings as fine aggregate in recycled aggregate concrete. *Journal of Cleaner Production*, Vol. 372, 2022, id. 133649.